Electronic coherences in nonadiabatic molecular photophysics revealed by time-resolved photoelectron spectroscopy

Stefano M. Cavaletto[a,b,1], Daniel Keefer[a,b,1], and Shaul Mukamel[a,b,1]

[a]Department of Chemistry, University of California, Irvine, CA 92697; and [b]Department of Physics & Astronomy, University of California, Irvine, CA 92697

Edited by Peter Rossky, Rice University, Houston, TX; received November 24, 2021; accepted January 19, 2022

Time-resolved photoelectron spectroscopy (TRPES) signals that monitor the relaxation of the RNA base uracil upon optical excitation are simulated. Distinguishable signatures of coherence dynamics at conical intersections are identified, with temporal and spectral resolutions determined by the duration of the ionizing probe pulse. The frequency resolution of the technique, either directly provided by the signal or retrieved at the data-processing stage, can magnify the contribution from molecular coherences, enabling the extraction of most valuable information about the nonadiabatic molecular dynamics. The predicted coherence signatures in TRPES could be experimentally observed with existing ultrashort pulses from high-order harmonic generation or free-electron lasers.

time-resolved photoelectron spectroscopy | molecular coherences | nonadiabatic dynamics | ultrafast science

The outcomes of virtually all photoinduced processes in molecules are determined by the strong coupling between electrons and nuclei at conical intersections (CoIns). At these degeneracy points between electronic potential energy surfaces, the electronic and nuclear frequencies become comparable, and the adiabatic Born–Oppenheimer approximation thus breaks down (1, 2). Observing CoIns in experiments has been particularly challenging due to demanding requirements on joint temporal and spectral resolutions (3, 4). With advancements in the generation of ultrashort extreme-ultraviolet (XUV) and X-ray pulses from high-order harmonic generation (HHG) and free-electron lasers (FELs) (5–8), a broad arsenal of experimental techniques has emerged for monitoring and imaging ultrafast molecular dynamical processes. These include high-harmonic spectroscopy (9), attosecond transient absorption (10–12), and ultrafast X-ray (13, 14) and electron diffraction (15, 16). Typically, these techniques do not provide background-free access to CoIns, as they possess contributions from level populations which are not as indicative of CoIns as the quantum coherences generated during these nonadiabatic passages. Stimulated Raman and X-ray diffraction techniques that can directly monitor quantum coherences have been investigated (17–22).

Here we show that time-resolved photoelectron spectroscopy (TRPES) is a particularly promising method for monitoring CoIns. In its long-time frequency-domain realization, this technique has long been used to access the level structure and ionization potentials of atoms, molecules, and materials (23). This is achieved by ionizing a material with an external field of suitable frequency, higher than the ionization potential, and measuring the kinetic energy distribution of the emitted photoelectrons. In photoelectron spectroscopy, photoionization due to the probe pulse constitutes the main process responsible for the signal, in contrast to stimulated Raman and X-ray diffraction techniques that measure the number of absorbed or emitted photons and where photoionization acts as a competing process that should be minimized. This renders photoelectron spectroscopy experimentally more accessible than the X-ray absorption techniques. In TRPES, dynamical information is obtained by varying the arrival time of an ultrashort ionizing pulse with respect to the initial pump (24–26). Recent advances employ XUV (27, 28) and X-ray pulses (29, 30). In these experiments, the signal provides access to the populations of the molecular states, and most theoretical methods interpret photoelectron spectra in terms of a semiclassical Fermi's golden rule, where the role of molecular coherences is entirely neglected (31–33).

Here we simulate TRPES signals to monitor the nonadiabatic dynamics of photoexcited uracil undergoing the passage through a CoIn and predict contributions from molecular coherences which could be distinguished with current technology. These coherence features, which directly emerge at the CoIn between the excited S_2 and the optically dark S_1 states in neutral uracil, provide unique temporal and spectral information regarding the nonadiabatic passage. We show that the duration of the probe pulse can be used to control the joint temporal and spectral resolution of the technique. For ultrashort attosecond pulses, we predict strong TRPES features due to the coherence between the ground S_0 and the bright S_2 excited state. Although the frequency resolution of the photoelectron signal is eroded for short broadband pulses, we show that a good time–frequency resolution can be recovered at the data-processing stage, by using Wigner or frequency resolved optical gating (FROG)-like spectrograms. Scanning the signal at sufficiently large frequencies allows one

Significance

Time-resolved photoelectron spectroscopy (TRPES) is a promising technique for the study of ultrafast molecular processes, such as the nonadiabatic dynamics taking place at conical intersections. Directly accessing the evolution of the coherences generated at the conical intersection should provide most valuable dynamical information. However, the signals are dominated by background contributions due to state populations, and most theoretical treatments completely neglect the role of the coherences. Here we show that distinguishable signatures of molecular coherences appear in TRPES. These can be recorded using currently available ultrashort pulses and unambiguously extracted at the postprocessing stage. The technique thus provides direct access to nonadiabatic coherence dynamics.

Author contributions: S.M.C., D.K., and S.M. designed research; S.M.C. and D.K. performed research; S.M.C., D.K., and S.M. analyzed data; and S.M.C., D.K., and S.M. wrote the paper.

The authors declare no competing interest.

This article is a PNAS Direct Submission.

This article is distributed under Creative Commons Attribution-NonCommercial-NoDerivatives License 4.0 (CC BY-NC-ND).

[1]To whom correspondence may be addressed. Email: smcavaletto@gmail.com, dkeefer@uci.edu, or smukamel@uci.edu.

Published March 7, 2022.

Downloaded from https://www.pnas.org by SCIENCE LIBRARY SERIALS on March 10, 2022 from IP address 128.200.11.4.

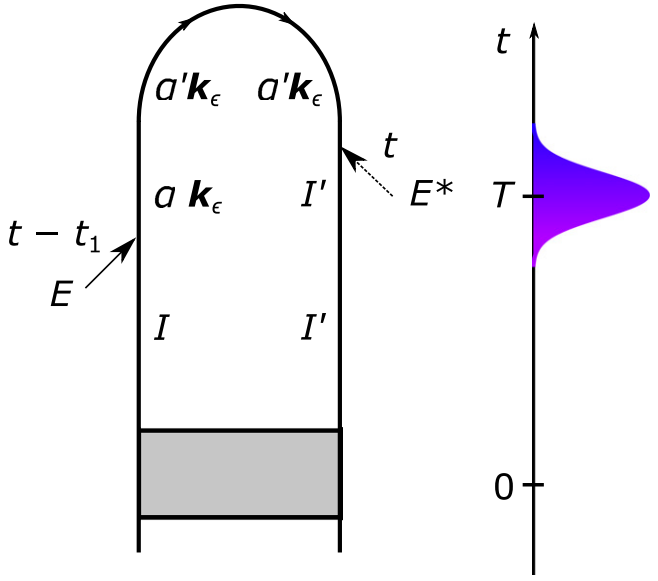

Fig. 1. Loop diagram of the photoelectron signal. The gray area represents the initial excitation of the neutral molecule around $t = 0$ and its subsequent nonadiabatic dynamics. *I* and *I*′ label adiabatic electronic states in the neutral molecule. The system is probed by a 20-eV attosecond or femtosecond ionizing pulse centered at $t = T$ (blue pulse on the right). The pulse acts both on the left and the right branches, at times $t - t_1$ and t, respectively. Both interaction times lie within the temporal envelope of the probe pulse. α and α' label nonadiabatic electronic states in the ionic molecule, while $\boldsymbol{k}_\epsilon$ labels a continuum state of the emitted photoelectron at the detected energy ϵ. Possible nonadiabatic dynamics in the time interval $[t - t_1, t]$ in the ionic molecule are accounted for in the diagram. These are not included in our simulations, which assume that the probe pulse is short compared to the dynamics in the ionic molecule.

to highlight the role of the coherence emerging at the CoIn and separate it from the population background.

The time-resolved photoelectron signal is represented by the loop diagram shown in Fig. 1. A neutral molecule is initially excited by a pump centered at $t = 0$, and its subsequent nonadiabatic dynamics are probed by an ionizing pulse centered at a variable time T. The evolution of the molecule prior to the ionizing pulse is described by the time-dependent wave function $|\Psi^{(0)}(t)\rangle = \sum_I |\chi_I(t)\rangle\,|\psi_I\rangle$, expanded in the adiabatic basis states $|\psi_I\rangle$ of the neutral molecule. $|\chi_I(t)\rangle$ is the time-dependent nuclear wave packet on the Ith potential energy surface. An ultrashort pulse $\boldsymbol{E}(t - T) = \hat{\boldsymbol{e}}\,E(t - T) = \hat{\boldsymbol{e}}\,\mathcal{E}(t - T)\,\mathrm{e}^{-\mathrm{i}\omega_\mathrm{X}(t-T)}$, of carrier frequency ω_X, polarization vector $\hat{\boldsymbol{e}}$, and envelope $\mathcal{E}(t)$, ionizes the molecule, leading to the emission of a photoelectron. We denote with $|\varphi_\alpha\rangle$ the αth adiabatic electronic states in the molecular ion, whereas $\boldsymbol{k}_\epsilon$ labels a continuum state of the emitted photoelectron with energy ϵ. The TRPES signal is obtained by energy dispersing the emitted photoelectrons as a function of the pulse arrival time T. The orientationally averaged signal

$$S(\epsilon,\,T) = S_\mathrm{pop}(\epsilon,\,T) + S_\mathrm{coh}(\epsilon,\,T) \qquad \textbf{[1]}$$

can then be partitioned into the sum of a population contribution ($I = I'$; Eq. **15**) and a coherence term ($I \neq I'$; Eq. **16**), as shown in *Materials and Methods*. The key molecular parameters required for computing the signal are the neutral $\omega_I(\boldsymbol{q})$ and ionic $\omega_\alpha(\boldsymbol{q})$ potential energy surfaces and the Dyson orbitals (34)

$$\phi_{\mathrm{D},\alpha I}(\boldsymbol{q},\boldsymbol{r}) = \sqrt{N}\int \mathrm{d}^3 r_2 \cdots \int \mathrm{d}^3 r_N\,\varphi^*_\alpha(\boldsymbol{q},\boldsymbol{r}_2,\ldots\boldsymbol{r}_N)\,\psi_I(\boldsymbol{q},\boldsymbol{r},\ldots\boldsymbol{r}_N), \qquad \textbf{[2]}$$

between the Ith and αth states, where $\boldsymbol{q} = (q_1,\ldots,q_M)$ is the vector of the M nuclear coordinates considered in the model.

For comparison, we note that the time-resolved photoelectron signal is most commonly simulated using a semiclassical expression $S_\mathrm{sc}(\epsilon,\,T)$ based on Fermi's golden rule (31–33),

$$S_\mathrm{sc}(\epsilon,\,T) = \int \mathrm{d}\omega\,|\tilde{\mathcal{E}}(\omega - \omega_\mathrm{X})|^2\,S_{\mathrm{sc},0}(\epsilon,\,T,\omega), \qquad \textbf{[3]}$$

where $\tilde{\mathcal{E}}(\omega)$ is the Fourier transform of the pulse envelope $\mathcal{E}(t)$ and

$$S_{\mathrm{sc},0}(\epsilon,\,T,\omega) = \sum_{I\alpha\boldsymbol{k}_\epsilon} \langle |\,\boldsymbol{V}_{\alpha\boldsymbol{k}_\epsilon,I}(\boldsymbol{q}(T))|^2\,n_I(\boldsymbol{q}(T)) \times \delta(\epsilon - \omega + \omega_\alpha(\boldsymbol{q}(T)) - \omega_I(\boldsymbol{q}(T)))\rangle \qquad \textbf{[4]}$$

is a reference signal for a fixed probe frequency ω, expanded on the adiabatic basis. The nuclear dynamics $\boldsymbol{q}(T)$ are simulated semiclassically, and $\langle\ldots\rangle$ denotes an average over the nuclear coordinates weighted by the populations $n_I(\boldsymbol{q}(T))$. As is apparent from Eqs. **3** and **4**, the semiclassical approach completely neglects contributions due to vibronic coherences. In the following, we show that these coherence terms lead to observable signatures in the TRPES signal.

We have calculated the photoelectron signal given by Eqs. **1**, **15**, and **16** to probe the photorelaxation of the RNA nucleobase uracil passing through a CoIn. Uracil has drawn significant attention, in both theory and experiment, because of its biological relevance, convenient size, and handleability. Various methods have been developed to calculate the photoexcited dynamics of coupled electronic and nuclear degrees of freedom at a CoIn. Traditional semiclassical surface-hopping approaches, where the nuclei are treated completely classically, miss the coherence emerging at the CoIn and therefore their signatures in the TRPES signal. More advanced semiclassical methods like ab initio multiple spawning (35) or cloning (36, 37) can capture these coherences and thus the complete TRPES signal. Another possibility is to aim for a more quantum description of the nuclear dynamics, e.g., through the multiconfigurational time-dependent Hartree method (38). Here we performed exact nuclear wave packet dynamics simulations in uracil, by using the effective Hamiltonian introduced in ref. 39 to include a completely quantum description of the nuclear degrees of freedom in the solution of the time-dependent Schrödinger equation. This model includes three adiabatic electronic states, and the dynamics are restricted to two nuclear coordinates q_1 and q_2, as shown in Fig. 2*A*: q_1 represents the motion from the Franck–Condon to the CoIn, whereas q_2 describes the motion from the Franck–Condon to a local minimum on the S_2 surface.

In Fig. 2*B*, we display the potential energy surfaces of the ground S_0 and the first two excited states S_1 and S_2 in neutral uracil, calculated at the CASSCF(12/8)/6-311G* level. There is a CoIn seam between S_1 and S_2 opening a radiationless relaxation pathway, as indicated by the black lines on the right bottom part of the panels in Fig. 2*B*. The ionization energies and Dyson orbitals were calculated adopting the approach described in ref. 32. Fig. 2*C* shows the ground D_0 and the first two excited-state surfaces D_1 and D_2 of cationic uracil (40). Their ionization energies from the minimum of the ground S_0 surface are centered between 8 and 10 eV, and the ionization energies from the neutral-molecule excited states S_1 and S_2 vary between 2 and 7 eV. These energies will appear in the photoelectron signal. Fig. 2*D* shows the spatial profile of the Dyson orbitals $\phi_{\mathrm{D},\alpha I}(\boldsymbol{r})$ (Eq. **2**) for the three neutral and ionic molecule states considered in our model and for a representative nuclear configuration, i.e., at the minimum of the S_2 surface at $q_1 = -0.2$ Å and $q_2 = 0.5$ Å. These orbitals exhibit the typical shape of valence molecular orbitals and correspond to the region in the molecule from which

Downloaded from https://www.pnas.org by SCIENCE LIBRARY SERIALS on March 10, 2022 from IP address 128.200.11.4.

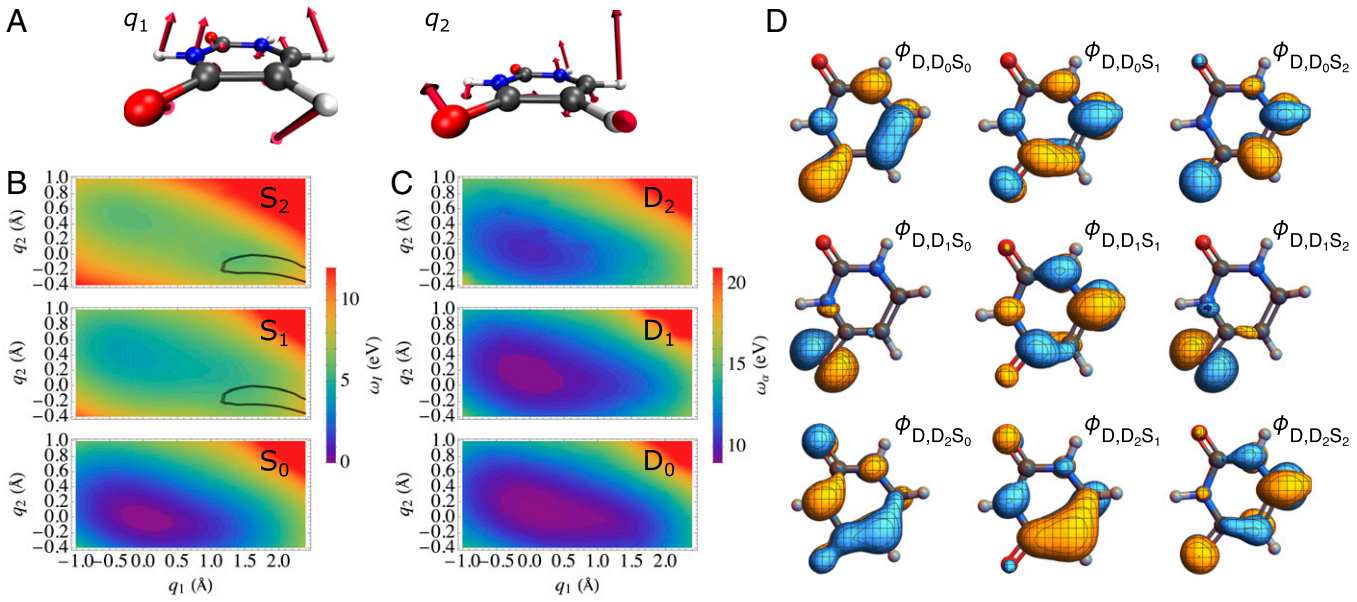

Fig. 2. (*A*) Uracil molecules at the ground-state minimum geometry, and the molecular displacement associated with the two degrees of freedom (*Left*) q_1 and (*Right*) q_2 included in the model. (*B*) Surfaces of neutral uracil, representing the ground state S_0 and the two excited states S_1 and S_2, as indicated in each panel. The black lines highlight the CoIn seam between the S_2 and S_1 potential energy surfaces. (*C*) Surfaces of ionic uracil, representing the ground state D_0 and the excited states D_1 and D_2, as indicated in each panel. Ionization energies are shown with respect to the minimum of the neutral-molecule S_0 state. (*D*) Dyson orbitals $\phi_{D,\alpha I}(r)$ (Eq. **2**) for the three ionic α and neutral *I* states considered, as indicated in each panel. The orbitals are displayed at the minimum geometry of the S_2 surface for $q_1 = -0.2$ Å and $q_2 = 0.5$ Å.

the electron is ejected upon ionization. They are mostly of π and π^* type, distributed across the entire molecular ring, with two oxygen lone pairs in the D_1S_0 and D_1S_2 transition.

The time-dependent wave function $|\Psi^{(0)}(t)\rangle$, representing the evolution of the neutral molecule prior to the ionizing probe pulse, is calculated for a 34-fs UV pump pulse centered at $t = 0$ and matching the $S_0 \rightarrow S_2$ transition energy, which transfers populations from S_0 into S_2. The associated populations and the S_2/S_1 coherence dynamics are shown in Fig. 3 *A* and *B*, respectively. After the pump excitation, the system freely evolves on the S_2 surface, until the wave packet reaches the CoIn, and the nonadiabatic passage takes place, starting at approximately $t = 100$ fs. This is reflected in the evolution of the populations and coherences: at the CoIn passage, some population is transferred from the S_2 into the S_1 state, thereby creating a vibronic coherence between these two states.

We simulate TRPES to probe the evolution of populations and coherences along this photophysical relaxation path in uracil. We assume a Gaussian XUV ionizing pulse centered at $\omega_X = 20$ eV and of envelope $\mathcal{E}(t) = e^{-t^2/(2\tau^2)}$. Fig. 4*A* presents the total photoelectron spectrum $S(\epsilon, T)$ for a probe pulse of duration $\tau = 1$ fs. The signal is dominated by populations (Eq. **15**), as is apparent in Fig. 4*B*, which displays the weaker coherence contribution $S_{coh}(\epsilon, T)$ due to $I \neq I'$ (Eq. **16**). The narrowband pulse used in Fig. 4 provides the frequency resolution needed to observe spectral changes due to the evolution of the molecular wave packet on the potential energy surface (41). The photoelectron energy peak reflects the local transition energy between the cationic and neutral states since $\epsilon \approx \omega_X - (\omega_\alpha - \omega_I)$ (see also Eqs. **3** and **4**). At negative time delays $T < 0$, when uracil is probed before the interaction with the pump, the signal is peaked at energies below 12 eV since the molecular wave packet is localized at the S_0 minimum. At positive time delays, after the pump has populated higher-energy excited states, the photoelectron signal shifts to higher energies, and its peak oscillates between 15.5 and 17 eV with an ~ 40 fs period. This oscillatory behavior is highlighted in Fig. 4*C*, which displays a section of the signal at $\epsilon_0 = 17.25$ eV. Its Fourier transform, depicted in Fig. 4*D*, clearly shows a 120 cm^{-1} peak, associated with the main mode of the nuclear motion. To examine how the photoelectron signal is linked to the underlying molecular dynamics, we present

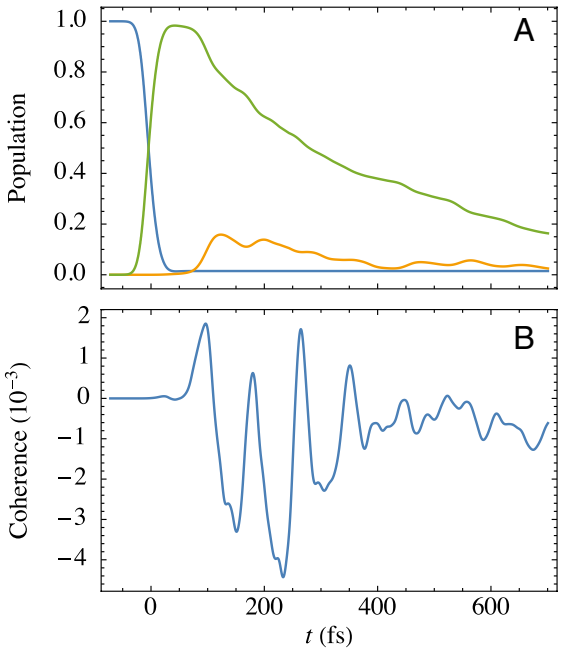

Fig. 3. Population and coherence dynamics of neutral uracil calculated for a 34-fs UV pump pulse centered at $t = 0$ and in resonance with the bright S_0 to S_2 transition. (*A*) The total populations in the (blue) S_0, (green) S_2, and (yellow) S_1 states show a population transfer from the S_0 to the S_2 states due to the pump pulse, a subsequent relaxation of the S_2 state, and the transfer of populations into the S_1 state due to the CoIn passage at around 100 fs. (*B*) Coherence between the S_2 and S_1 states generated at the CoIn passage.

Downloaded from https://www.pnas.org by SCIENCE LIBRARY SERIALS on March 10, 2022 from IP address 128.200.11.4.

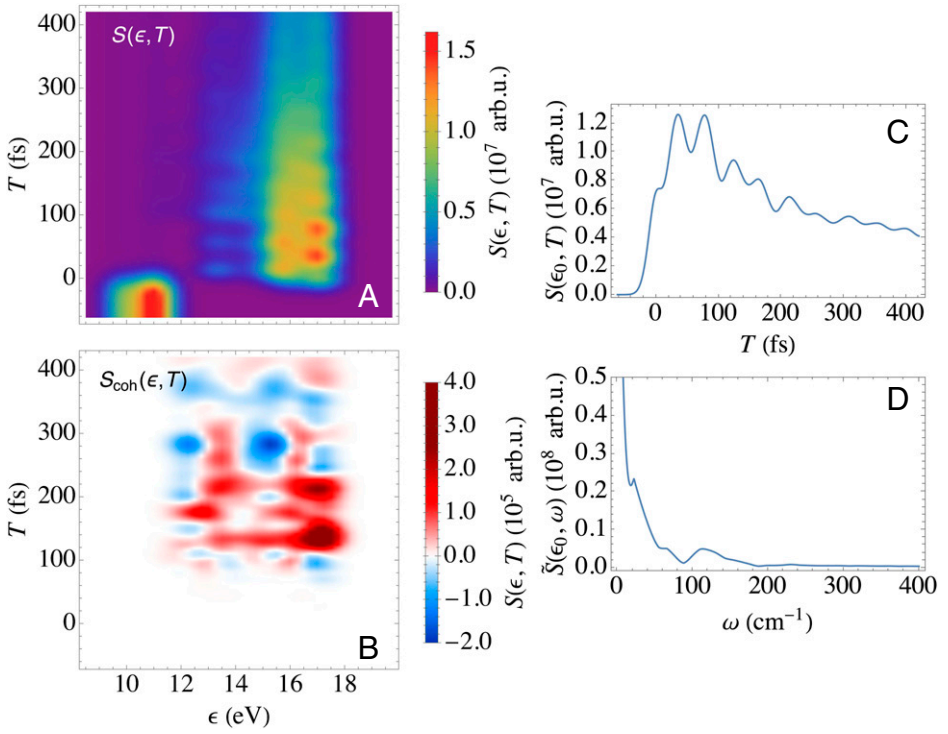

Fig. 4. TRPES signal for a 20-eV probe pulse of duration $\tau = 1$ fs. (*A*) Total signal $S(\epsilon, \mathrm{T})$, (*B*) coherence contribution $S_{\mathrm{coh}}(\epsilon, T)$ (Eq. **16**), (*C*) section of the signal $S(\epsilon, \mathrm{T})$ in *A* evaluated at $\epsilon_0 = 17.25$ eV, and (*D*) its Fourier transform $\tilde{S}(\epsilon_0, \omega)$.

in Fig. 5 contour plots of the molecular wave packet at three representative time delays T separated by 20 fs. The panels also show the corresponding value of the ionization energy $(\omega_{\mathrm{D}_0}(\boldsymbol{q}) - \omega_{\mathrm{S}_2}(\boldsymbol{q}))$ from the neutral S_2 to the ionic D_0 state. We see that the wave packet moves between regions in nuclear space associated with different ionization energies. These nuclear dynamics are encoded in the time dependence of the photoelectron signal in Fig. 4*A*. Additional spectral features, for example, at energies ϵ of 14 eV, are due to the other photoionization pathways, corresponding to the D_1 and D_2 excited states of the cation.

Fig. 4*B* depicts the coherence contribution $S_{\mathrm{coh}}(\epsilon, T)$ (Eq. **16**). The signal encodes the evolution of the $\mathrm{S}_2/\mathrm{S}_1$ coherence emerging during the CoIn passage at approximately $T = 100$ fs (see also Fig. 3). For this coherence term to contribute to the photoelectron signal, the pulse bandwidth has to be broader than the transition energy between states S_2 and S_1. Only then can the excitations depicted on the left and on the right branches of the loop diagram in Fig. 1 take place, corresponding to the two ionization pathways from different states I and I' to the ionic state α. The coherence signal in Fig. 4*B* is very broad in energy as it is the sum of three ionization pathways to the three α cationic states. Note that $S_{\mathrm{coh}}(\epsilon, T)$ can be positive or negative, leading to an increase or decrease in the total photoelectron signal, respectively. This sign reflects the evolution and phase of the associated molecular coherence. Fig. 4*B* shows that the coherence contribution to the signal is weaker than that due to populations, reflecting the relative magnitude of the populations and coherences in Fig. 3. The emerging coherence between the S_1 and S_2 states is $\sim$1/100 of the total populations. We stress that this ratio, albeit small, could be distinguished at the current experimental detection limit ($\approx 0.05\%$) (14). Furthermore, the 34-fs UV pump pulse used in this case was chosen to transfer populations without any optimization, but quantum-control techniques could be employed to optimize the pump pulse spectral and temporal features, and thus maximize the coherence contribution (42). Alternatively, molecules with more localized nuclear wave packets passing through the CoIn would exhibit a larger and longer-lived coherence and would thus enhance the coherence signature in the TRPES signal. The standard semiclassical approaches typically used to predict photoelectron spectroscopy signals (31–33) do not account for molecular coherences and thus miss these experimentally accessible signatures.

The role of coherences in TRPES is further highlighted in Fig. 6, which displays the total signal $S(\epsilon, T)$ and its two components $S_{\mathrm{pop}}(\epsilon, T)$ and $S_{\mathrm{coh}}(\epsilon, T)$ for an ultrashort probe pulse of $\tau = 200$ as. The signal is displayed for time delays centered around $T = 0$ fs. Due to the very broad bandwidth of the attosecond probe pulse used, the photoelectron signal shows very broad lines with poor spectral resolution. The contributions of different neutral and ionic states, which could be distinguished in Fig. 4, are now convolved underneath the large probe pulse bandwidth. At the same time, the attosecond probe pulse employed here is broader than the transition energy between S_0 and S_2. Because of this, the total photoelectron signal in Fig. 6*A* contains clearly distinguishable signatures stemming from the coherence between these two states. This is further highlighted by comparing the population $S_{\mathrm{pop}}(\epsilon, T)$ and coherence $S_{\mathrm{coh}}(\epsilon, T)$ contributions in Fig. 6 *B* and *C*, respectively. The $\mathrm{S}_0/\mathrm{S}_2$ coherence shown in the photoelectron signal is created during the pump excitation, in contrast to the more informative $\mathrm{S}_1/\mathrm{S}_2$ coherence created by the passage through the CoIn and discussed in Fig. 4. The wave packets in the S_0 and S_2 surfaces have a significant overlap, corresponding to a larger coherence than the one generated at the CoIn between S_2 and S_1. The amplitude of the $\mathrm{S}_0/\mathrm{S}_2$ coherence is comparable to the populations, leading to discernible features in the total photoelectron signal. We here assumed an ultrashort probe pulse with very good control over its jitter and arrival time. Thereby, $S_{\mathrm{coh}}(\epsilon, T)$ allows one to follow the time dependence of this $\mathrm{S}_0/\mathrm{S}_2$ coherence and its oscillation between positive and negative values with high temporal resolution. The frequency of these fast coherence oscillations reflects the large transition energy between the S_0 and S_2 states.

Downloaded from https://www.pnas.org by SCIENCE LIBRARY SERIALS on March 10, 2022 from IP address 128.200.11.4.

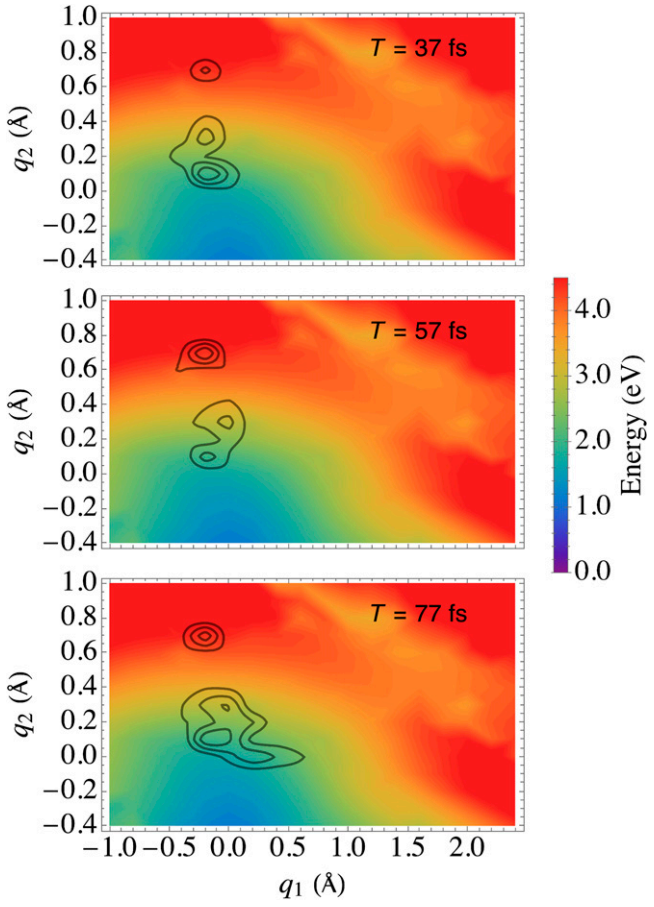

Fig. 5. Evolution of the molecular wave packet in two-dimensional nuclear space. The black lines represent contour plots of the molecular wave packet at the three representative time delays T indicated in each panel: (*Top*) T = 37 fs, (*Middle*) T = 57 fs, and (*Bottom*) T = 77 fs. The corresponding value of the ionization energy $(\omega_{D_0}(q) - \omega_{S_2}(q))$ from the neutral S_2 to the ionic D_0 state is displayed in the background of each panel.

High temporal and spectral resolution about CoIn dynamics from jittery, stochastic FEL pulses could also be obtained at the data-processing stage by a correlation analysis (19, 22) or machine learning (43), as recently proposed and investigated experimentally.

The good temporal resolution provided by the ultrashort probe pulse used in Fig. 6 can follow even the fast oscillations in the S_2/S_0 coherence. However, it does not offer high spectral resolution, rendering it difficult to separate and monitor coherences emerging from different sets of electronic states (41). Proposals to improve the temporal and spectral resolutions by means of trains of attosecond pulses have been made recently (44). Here, in order to retrieve the spectral information from temporally well-resolved data, in Fig. 7 we display the FROG spectrogram of the photoelectron signal $S(\epsilon_0, T)$ (Eqs. **1**, **15**, and **16**) calculated for $\tau = 200$ fs and evaluated at $\epsilon_0 = 17.25$ eV. This spectrogram can be generated by a postprocessing analysis of the photoelectron signal $S(\epsilon_0, T')$ for a given ϵ_0, by taking the Fourier transform

$$W(\omega_{\mathrm{FROG}}, T) = \left| S(\epsilon_0, T')\, G_{\mathrm{gate}}(T - T')\, \mathrm{e}^{-\mathrm{i}\omega_{\mathrm{FROG}} T'}\, \mathrm{d}T' \right|. \quad [5]$$

Here $G_{\mathrm{gate}}(T) = \mathrm{e}^{-T^2/(2\tau_{\mathrm{gate}}^2)}$ is a narrowband gate function used for data processing, with duration here set equal to $\tau_{\mathrm{gate}} = 15$ fs, and does not require additional measurements. The energy ϵ_0 was chosen so that it lies within the broad spectral peak of the photoelectron signal. Since the signal in Fig. 6 possesses very broad spectral features, one could have alternatively considered the FROG spectrogram of the energy-integrated signal, which would not require energy dispersion and could thus be more easily measured.

The spectrogram is shown in Fig. 7 within a relatively narrow region centered on $\omega_{\mathrm{FROG}} = 0$ eV. Higher-frequency components, due, for instance, to the S_2/S_0 coherence, do not appear in this spectral region. The spectrogram of the total photoelectron signal is dominated by the slow evolution of the populations, which appear in Fig. 7*A* as a main peak

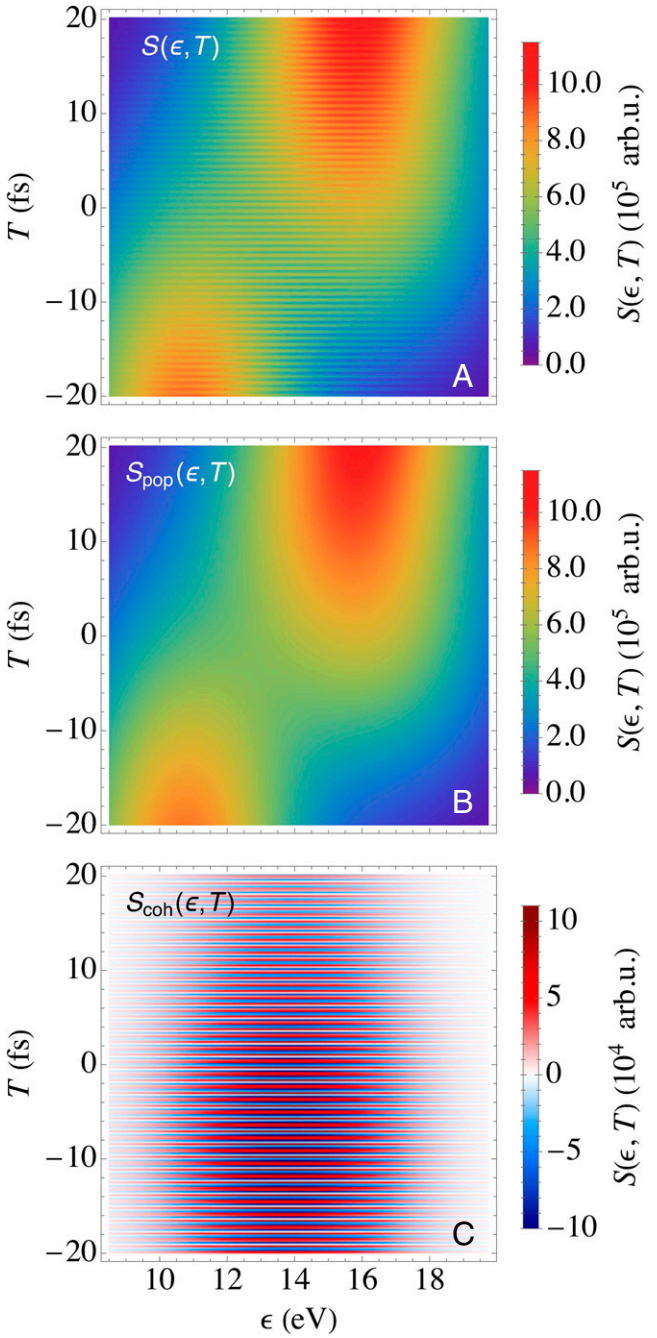

Fig. 6. TRPES signal for a 20-eV probe pulse of duration $\tau = 200$ as. The signal is shown for time delays around $T = 0$ fs. (*A*) The total signal $S(\epsilon, T)$ and contributions from (*B*) populations $S_{\mathrm{pop}}(\epsilon, T)$ (Eq. **15**) and (*C*) coherences $S_{\mathrm{coh}}(\epsilon, T)$ (Eq. **16**) are exhibited.

Downloaded from https://www.pnas.org by SCIENCE LIBRARY SERIALS on March 10, 2022 from IP address 128.200.11.4.

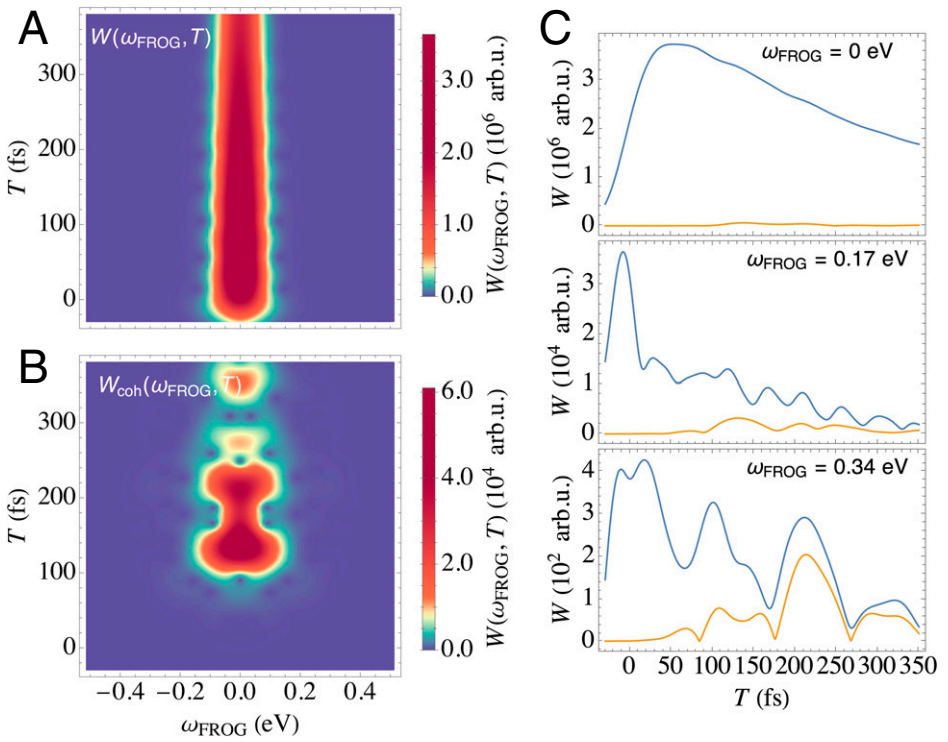

Fig. 7. FROG spectrogram $W(\omega_{FROG}, T)$ (Eq. **5**) of the time-resolved photoelectron signal $S(\epsilon_0, T)$ evaluated at $\epsilon_0 = 17.25$ eV and obtained with a 20-eV probe pulse of duration $\tau = 200$ as. The FROG spectrogram is calculated assuming a Gaussian gate window of duration $\tau_{gate} = 15$ fs. (*A*) FROG spectrogram $W(\omega_{FROG}, T)$ of the total photoelectron signal, (*B*) FROG spectrogram $W_{coh}(\omega_{FROG}, T)$ of the coherence contribution $S_{coh}(\epsilon_0, T)$, and (*C*) sections of the (blue) total FROG spectrogram $W(\omega_{FROG}, T)$ in *A* and of the (yellow) coherent contribution to the spectrogram $W_{coh}(\omega_{FROG}, T)$ in *B* at indicated values of ω_{FROG}.

centered around $\omega_{\mathrm{FROG}} = 0\,\mathrm{eV}$. The contribution from the S_2/S_1 coherence emerging at the CoIn is highlighted in Fig. 7*B*, which exhibits the spectrogram $W_{\mathrm{coh}}(\omega_{\mathrm{FROG}}, T)$ calculated exclusively from $S_{\mathrm{coh}}(\epsilon, T)$ (Eq. **16**). The spectral resolution enabled by the spectrogram allows us to highlight the weak contribution of the S_2/S_1 coherence, as apparent in the sections presented in Fig. 7*C*. At $\omega_{\mathrm{FROG}} = 0$, the spectrogram essentially reflects the dynamics of the populations, which evolve slowly in time and thus dominate the spectrum at small values of ω_{FROG}. Upon increasing ω_{FROG}, for instance, at $\omega_{\mathrm{FROG}} = 0.17\,\mathrm{eV}$ and then at $\omega_{\mathrm{FROG}} = 0.34\,\mathrm{eV}$, the population contribution diminishes, and the role of the S_2/S_1 coherences in the total spectrogram becomes clearly apparent. This is analogous to the frequency-resolved ultrafast X-ray diffraction setup recently proposed in ref. 22, where the contributions from populations and coherences could be similarly distinguished via frequency dispersion of the signal. By exploiting the joint temporal and spectral resolution of the technique, key information about the spectral distribution across the CoIn passage is provided.

To summarize, TRPES was applied to the nonadiabatic dynamics of uracil after excitation by a pump pulse in a simulation study. A 1-fs 20-eV probe pulse was first assumed, providing the joint temporal and spectral resolution to monitor the wave packet evolution spanning the relevant regions in nuclear space. A contribution due to the S_2/S_1 coherences was identified, which could be observed with existing spectrometers and could be enhanced by means of a suitably shaped pump pulse. For a shorter 200-as probe pulse, clear coherence signatures due to the wave packet overlap between the S_0 and S_2 surfaces were predicted. Attosecond pulses were shown to provide high temporal resolution of time-resolved photoelectron signals, at the expenses of lower spectral resolution. Valuable spectral resolution was retrieved by an analysis based on FROG spectrograms, which allowed us to highlight the coherence contribution at sufficiently large frequencies ω_{FROG}.

Advances in HHG- and FEL-based light sources are now providing ultrashort broadband pulses, opening up an entirely new regime of time-resolved investigations. We showed that experimentally detectable features appear in the time-resolved photoelectron signal, which are completely missed by the standard semiclassical formulation based on Fermi's golden rule and require the inclusion of coherence contributions. Distinguishing these contributions in TRPES will provide a background-free probe of nonadiabatic dynamics, better indicative of CoIns than the contributions from state populations. Our simulations for uracil undergoing nonadiabatic dynamics highlight the key role of molecular coherences for future theory and experimental TRPES investigations.

Materials and Methods

Derivation of the Time-Resolved Photoelectron Signal. We consider a molecule initially in a neutral state, described by the Hamiltonian

$$\hat{H}_{\mathrm{neutral}} = \sum_I \hat{H}_I |\psi_I\rangle\langle\psi_I| + \sum_{I' \neq I} \hat{H}_{II'} |\psi_I\rangle\langle\psi_{I'}|, \qquad [6]$$

where I and I' label the adiabatic electronic states $|\psi_I\rangle$ of the neutral molecule, and the operators $\hat{H}_I$ and $\hat{H}_{II'}$ act on the nuclear space. A probe pulse, centered at time T as depicted in Fig. 1, ionizes the molecules, producing an ion with the Hamiltonian

$$\hat{H}_{\mathrm{ion}} = \sum_\alpha \hat{H}_\alpha |\varphi_\alpha\rangle\langle\varphi_\alpha| + \sum_{\alpha' \neq \alpha} \hat{H}_{\alpha\alpha'} |\varphi_\alpha\rangle\langle\varphi_{\alpha'}|, \qquad [7]$$

where α and α' now label the adiabatic electronic states $|\varphi_\alpha\rangle$ of the ionic molecule, and $\hat{H}_\alpha$ and $\hat{H}_{\alpha\alpha'}$ act on the corresponding nuclear space. We neglect the effect of the Coulomb potential of the molecular ion on the free electron, which is thus described by the Hamiltonian

$$\hat{H}_{\mathrm{free}} = \sum_k \epsilon_k |\phi_k\rangle\langle\phi_k|, \qquad [8]$$

where k runs over the continuum states $|\phi_k\rangle$ of energy $\epsilon_k = k^2/2$. The photoionization process is described by the light–matter interaction Hamiltonian

Downloaded from https://www.pnas.org by SCIENCE LIBRARY SERIALS on March 10, 2022 from IP address 128.200.11.4.

$$\hat{H}_{\text{int}} = -\boldsymbol{E}(t-T)\cdot\hat{\boldsymbol{V}}^{\dagger} - \boldsymbol{E}^{*}(t-T)\cdot\hat{\boldsymbol{V}}, \quad [9]$$

with the electric field $\boldsymbol{E}(t) = \hat{e}\,E(t) = \hat{e}\,\mathcal{E}(t)\,\mathrm{e}^{-\mathrm{i}\omega_X t}$, and the dipole operator in the rotating-wave approximation

$$\hat{V} = \sum_{l\alpha k} \hat{V}_{l,\alpha k}\,|\psi_l\rangle\langle\varphi_\alpha\phi_k|. \quad [10]$$

Here $\hat{V}_{l,\alpha k}$ is a matrix element over the electronic degrees of freedom but is still an operator in the nuclear space of the neutral and ionic molecules.

The photoelectron signal is defined as the integrated rate of change of the number $\hat{N}_\epsilon$ of photoelectrons with energy ϵ,

$$S(\epsilon)\mathrm{d}\epsilon = \int \left\langle \frac{\mathrm{d}\hat{N}_\epsilon}{\mathrm{d}t} \right\rangle \mathrm{d}t. \quad [11]$$

Using Heisenberg's equations of motion and the interaction Hamiltonian in Eq. **9**, we calculate the signal in Eq. **11**, which gives

$$S(\epsilon,T) = 2\mathbf{Im}\Big\{\int \mathrm{d}t\,E^{*}(t-T)\,\sqrt{2\epsilon}\int \mathrm{d}\Omega_{k_\epsilon}\sum_{l'\alpha'} \times \mathrm{Tr}\Big\{\hat{e}^{*}\cdot\hat{V}_{l',\alpha' k_\epsilon}\,|\psi_{l'}\rangle\langle\varphi_{\alpha'}\phi_{k_\epsilon}|\,\hat{\rho}^{(1)}(t)\Big\}\Big\}. \quad [12]$$

Here the integration over the solid angle $\mathrm{d}\Omega_{k_\epsilon}$ is limited to photoelectron states $\phi_{k_\epsilon}(r) = \mathrm{e}^{-\mathrm{i}k_\epsilon\cdot r}/\sqrt{(2\pi)^3}$ of energy ϵ, and $\hat{\rho}^{(1)}(t)$ is the density matrix to first order in the ionizing pulse.

To derive a closed-form expression for the signal, we introduce the time-dependent density matrix $\hat{\rho}^{(0)}(t) = |\Psi^{(0)}(t)\rangle\langle\Psi^{(0)}(t)|$ of the neutral molecule prior to the ionizing pulse, written in terms of the time-dependent wave function $|\Psi^{(0)}(t)\rangle$, and further introduce the Green's function of the generated ion

$$\hat{G}(t,t_0) = \sum_{\alpha\alpha'} \hat{G}_{\alpha'\alpha}(t,t_0)\,|\varphi_{\alpha'}\rangle\langle\varphi_\alpha|, \quad [13]$$

written in terms of the operator $\hat{G}_{\alpha'\alpha}(t,t_0)$ acting on the nuclear space. The free evolution of a photoelectron $|\phi_{k_\epsilon}\rangle$ of energy ϵ is given by the Green's function $\mathrm{e}^{-\mathrm{i}\epsilon(t-t_0)}|\phi_{k_\epsilon}\rangle\langle\phi_{k_\epsilon}|$. The photoelectron signal can thus be recast as

$$S(\epsilon,T) = 2\mathbf{Re}\Big\{\int \mathrm{d}t\int_0^\infty \mathrm{d}t_1\,\mathcal{E}^{*}(t-T)\,\mathcal{E}(t-t_1-T) \times \mathrm{e}^{-\mathrm{i}(\epsilon-\omega_X)t_1}\sum_{ll'}\sum_{\alpha\alpha'}\sqrt{2\epsilon}\int \mathrm{d}\Omega_{k_\epsilon}\,\langle\chi_{l'}(t)|\,\hat{e}^{*}\cdot\hat{V}_{l',\alpha' k_\epsilon} \times \hat{G}_{\alpha'\alpha}(t,t-t_1)\,\hat{e}\cdot\hat{V}_{\alpha k_\epsilon,l}\,|\chi_l(t-t_1)\rangle\Big\} \quad [14]$$

and can be partitioned into the sum of a population $S_{\text{pop}}(\epsilon,T)$ ($l = l'$) and a coherence contribution $S_{\text{coh}}(\epsilon,T)$ ($l \neq l'$).

The evolution of the molecular wave packet $\chi_l(q,t)$ was obtained by solving the Schrödinger equation for the neutral molecule surfaces $\omega_l(q)$, where q is the vector of the nuclear coordinates considered in the model.

Furthermore, the Green's function $G_{\alpha'\alpha}(q,t,t-t_1) \approx \mathrm{e}^{-\mathrm{i}\omega_\alpha(q)t_1}\delta_{\alpha'\alpha}$ was approximated locally in terms of the ionic molecule surfaces $\omega_\alpha(q)$, assuming that its time dependence is slow compared to the duration of the ionizing pulse and that dynamics on different ionic potential energy surfaces are not coupled during this short pulse duration. With the above assumptions, the orientationally averaged population and coherence contributions to the photoelectron signal can be recast as

$$S_{\text{pop}}(\epsilon,T) = 2\mathbf{Re}\Big\{\int \mathrm{d}t\int_0^\infty \mathrm{d}t_1\,\mathcal{E}^{*}(t-T)\,\mathcal{E}(t-t_1-T) \times \mathrm{e}^{-\mathrm{i}(\epsilon-\omega_X)t_1}\sum_{l}\sum_{\alpha}\sum_{i}\int \mathrm{d}^M q\,\frac{\sqrt{2\epsilon}}{3}\int \mathrm{d}\Omega_{k_\epsilon}\,\chi_l^{*}(q,t) \times \hat{e}_i^{*}\cdot\boldsymbol{V}_{l,\alpha k_\epsilon}(q)\,\mathrm{e}^{-\mathrm{i}\omega_\alpha(q)t_1}\,\hat{e}_i\cdot\boldsymbol{V}_{\alpha k_\epsilon,l}(q)\,\chi_l(q,t-t_1)\Big\} \quad [15]$$

and

$$S_{\text{coh}}(\epsilon,T) = 2\mathbf{Re}\Big\{\int \mathrm{d}t\int_0^\infty \mathrm{d}t_1\,\mathcal{E}^{*}(t-T)\,\mathcal{E}(t-t_1-T) \times \mathrm{e}^{-\mathrm{i}(\epsilon-\omega_X)t_1}\sum_{l\neq l'}\sum_{\alpha}\sum_{i}\int \mathrm{d}^M q\,\frac{\sqrt{2\epsilon}}{3}\int \mathrm{d}\Omega_{k_\epsilon}\,\chi_{l'}^{*}(q,t) \times \hat{e}_i^{*}\cdot\boldsymbol{V}_{l',\alpha k_\epsilon}(q)\,\mathrm{e}^{-\mathrm{i}\omega_\alpha(q)t_1}\,\hat{e}_i\cdot\boldsymbol{V}_{\alpha k_\epsilon,l}(q)\,\chi_l(q,t-t_1)\Big\}, \quad [16]$$

respectively, where the unit vector $\hat{e}_i$ runs over the three directions x, y, and z. The transition dipole matrix elements

$$\boldsymbol{V}_{\alpha k,l}(q) \doteq \langle\varphi_\alpha(q,r_2,\ldots,r_N)\phi_k(r_1)| \times \hat{V}(q,r_1,\ldots,r_N)|\psi_l(q,r_1,\ldots,r_N)\rangle \quad [17]$$

are defined in terms of the eigenstates of the neutral N- and ionic $(N-1)$-electron systems. Due to the orthogonality between the cation and continuum electrons, the matrix element can be approximated as

$$\boldsymbol{V}_{\alpha k,l}(q) \approx \int \mathrm{d}^3 r\,\frac{\mathrm{e}^{\mathrm{i}k\cdot r}}{\sqrt{(2\pi)^3}}\,r\,\phi_{\mathrm{D},\alpha l}(q,r) \quad [18]$$

in terms of the Dyson orbitals $\phi_{\mathrm{D},\alpha l}(q,r)$ in Eq. **2**.

Data Availability. All study data are included in the article.

ACKNOWLEDGMENTS. We gratefully acknowledge the support of the Chemical Sciences, Geosciences, and Biosciences division, Office of Basic Energy Sciences, Office of Science, US Department of Energy (DOE), through Award DE-SC0019484 (S.M.C. and S.M.) and of the NSF (Grant CHE-1953045). D.K. gratefully acknowledges support from the Alexander von Humboldt foundation through the Feodor Lynen program. We thank Markus Kowalewski for providing his QDng quantum dynamics code.

1. G. A. Worth, L. S. Cederbaum, Beyond Born-Oppenheimer: Molecular dynamics through a conical intersection. *Annu. Rev. Phys. Chem.* **55**, 127–158 (2004).
2. W. Domcke, D. R. Yarkony, H. Köppel, *Conical Intersections* (Advanced Series in Physical Chemistry, World Scientific, Singapore, 2011), vol. 17, pp. i–xiii.
3. D. Polli *et al.*, Conical intersection dynamics of the primary photoisomerization event in vision. *Nature* **467**, 440–443 (2010).
4. B. K. McFarland *et al.*, Ultrafast X-ray Auger probing of photoexcited molecular dynamics. *Nat. Commun.* **5**, 4235 (2014).
5. F. Krausz, M. Ivanov, Attosecond physics. *Rev. Mod. Phys.* **81**, 163 (2009).
6. C. Pellegrini, A. Marinelli, S. Reiche, The physics of X-ray free-electron lasers. *Rev. Mod. Phys.* **88**, 015006 (2016).
7. J. Duris *et al.*, Tunable isolated attosecond X-ray pulses with gigawatt peak power from a free-electron laser. *Nat. Photonics* **14**, 30–36 (2020).
8. P. K. Maroju *et al.*, Attosecond pulse shaping using a seeded free-electron laser. *Nature* **578**, 386–391 (2020).
9. H. J. Wörner *et al.*, Conical intersection dynamics in NO_2 probed by homodyne high-harmonic spectroscopy. *Science* **334**, 208–212 (2011).
10. Y. Kobayashi, K. F. Chang, T. Zeng, D. M. Neumark, S. R. Leone, Direct mapping of curve-crossing dynamics in IBr by attosecond transient absorption spectroscopy. *Science* **365**, 79–83 (2019).
11. H. Timmers *et al.*, Disentangling conical intersection and coherent molecular dynamics in methyl bromide with attosecond transient absorption spectroscopy. *Nat. Commun.* **10**, 3133 (2019).
12. K. S. Zinchenko *et al.*, Sub-7-femtosecond conical-intersection dynamics probed at the carbon K-edge. *Science* **371**, 489–494 (2021).
13. J. M. Glownia *et al.*, Self-referenced coherent diffraction X-ray movie of ångstrom- and femtosecond-scale atomic motion. *Phys. Rev. Lett.* **117**, 153003 (2016).
14. B. Stankus *et al.*, Ultrafast X-ray scattering reveals vibrational coherence following Rydberg excitation. *Nat. Chem.* **11**, 716–721 (2019).
15. T. J. A. Wolf *et al.*, The photochemical ring-opening of 1,3-cyclohexadiene imaged by ultrafast electron diffraction. *Nat. Chem.* **11**, 504–509 (2019).
16. J. Yang *et al.*, Simultaneous observation of nuclear and electronic dynamics by ultrafast electron diffraction. *Science* **368**, 885–889 (2020).
17. M. Kowalewski, K. Bennett, K. E. Dorfman, S. Mukamel, Catching conical intersections in the act: Monitoring transient electronic coherences by attosecond stimulated X-ray Raman signals. *Phys. Rev. Lett.* **115**, 193003 (2015).
18. D. Keefer, T. Schnappinger, R. de Vivie-Riedle, S. Mukamel, Visualizing conical intersection passages via vibronic coherence maps generated by stimulated ultrafast X-ray Raman signals. *Proc. Natl. Acad. Sci. U.S.A.* **117**, 24069–24075 (2020).
19. S. M. Cavaletto, D. Keefer, S. Mukamel, High temporal and spectral resolution of stimulated X-ray raman signals with stochastic free-electron-laser pulses. *Phys. Rev. X* **11**, 011029 (2021).
20. K. Bennett, M. Kowalewski, J. R. Rouxel, S. Mukamel, Monitoring molecular nonadiabatic dynamics with femtosecond X-ray diffraction. *Proc. Natl. Acad. Sci. U.S.A.* **115**, 6538–6547 (2018).
21. D. Keefer *et al.*, Imaging conical intersection dynamics during azobenzene photoisomerization by ultrafast X-ray diffraction. *Proc. Natl. Acad. Sci. U.S.A.* **118**, e2022037118 (2021).
22. S. M. Cavaletto *et al.*, Unveiling the spatial distribution of molecular coherences at conical intersections by covariance X-ray diffraction signals. *Proc. Natl. Acad. Sci. U.S.A.* **118**, e2105046118 (2021).

Downloaded from https://www.pnas.org by SCIENCE LIBRARY SERIALS on March 10, 2022 from IP address 128.200.11.4.

23. A. Wendel, W. Pilz, R. Ladenstein, G. Sawatzki, U. Weser, Substrate-induced redox change of selenium in glutathione peroxidase studied by X-ray photoelectron spectroscopy. *Biochim. Biophys. Acta* **377**, 211–215 (1975).
24. D. M. Neumark, Time-resolved photoelectron spectroscopy of molecules and clusters. *Annu. Rev. Phys. Chem.* **52**, 255–277 (2001).
25. A. Stolow, A. E. Bragg, D. M. Neumark, Femtosecond time-resolved photoelectron spectroscopy. *Chem. Rev.* **104**, 1719–1757 (2004).
26. M. Wollenhaupt, V. Engel, T. Baumert, Femtosecond laser photoelectron spectroscopy on atoms and small molecules: Prototype studies in quantum control. *Annu. Rev. Phys. Chem.* **56**, 25–56 (2005).
27. A. von Conta *et al.*, Conical-intersection dynamics and ground-state chemistry probed by extreme-ultraviolet time-resolved photoelectron spectroscopy. *Nat. Commun.* **9**, 3162 (2018).
28. T. J. A. Wolf *et al.*, Observation of ultrafast intersystem crossing in thymine by extreme ultraviolet time-resolved photoelectron spectroscopy. *J. Phys. Chem. A* **123**, 6897–6903 (2019).
29. F. Braußе *et al.*, Time-resolved inner-shell photoelectron spectroscopy: From a bound molecule to an isolated atom. *Phys. Rev. A (Coll. Park)* **97**, 043429 (2018).
30. D. Mayer *et al*., Following excited-state chemical shifts in molecular ultrafast X-ray photoelectron spectroscopy. *Nat. Commun*. **13**, 198 (2022).
31. H. R. Hudock *et al*., Ab initio molecular dynamics and time-resolved photoelectron spectroscopy of electronically excited uracil and thymine. *J. Phys. Chem. A* **111**, 8500–8508 (2007).
32. W. J. Glover *et al.*, Excited state non-adiabatic dynamics of the smallest polyene, trans 1,3-butadiene. II. Ab initio multiple spawning simulations. *J. Chem. Phys.* **148**, 164303 (2018).
33. P. Chakraborty, Y. Liu, S. McClung, T. Weinacht, S. Matsika, Time resolved photoelectron spectroscopy as a test of electronic structure and nonadiabatic dynamics. *J. Phys. Chem. Lett.* **12**, 5099–5104 (2021).
34. C. M. Oana, A. I. Krylov, Dyson orbitals for ionization from the ground and electronically excited states within equation-of-motion coupled-cluster formalism: Theory, implementation, and examples. *J. Chem. Phys.* **127**, 234106 (2007).
35. M. Ben-Nun, J. Quenneville, T. J. Martínez, Ab initio multiple spawning: Photochemistry from first principles quantum molecular dynamics. *J. Phys. Chem. A* **104**, 5161–5175 (2000).
36. D. V. Makhov, W. J. Glover, T. J. Martínez, D. V. Shalashilin, Ab initio multiple cloning algorithm for quantum nonadiabatic molecular dynamics. *J. Chem. Phys.* **141**, 054110 (2014).
37. D. Keefer *et al.*, Monitoring molecular vibronic coherences in a bichromophoric molecule by ultrafast X-ray spectroscopy. *Chem. Sci. (Camb.)* **12**, 5286–5294 (2021).
38. G. A. Worth, H.-D. Meyer, H. Köppel, L. S. Cederbaum, I. Burghardt, Using the mctdh wavepacket propagation method to describe multimode non-adiabatic dynamics. *Int. Rev. Phys. Chem.* **27**, 569–606 (2008).
39. D. Keefer, S. Thallmair, S. Matsika, R. de Vivie-Riedle, Controlling photorelaxation in uracil with shaped laser pulses: A theoretical assessment. *J. Am. Chem. Soc.* **139**, 5061–5066 (2017).
40. M. Assmann, T. Weinacht, S. Matsika, Surface hopping investigation of the relaxation dynamics in radical cations. *J. Chem. Phys.* **144**, 034301 (2016).
41. K. Bennett, M. Kowalewski, S. Mukamel, Nonadiabatic dynamics may be probed through electronic coherence in time-resolved photoelectron spectroscopy. *J. Chem. Theory Comput.* **12**, 740–752 (2016).
42. D. Keefer, S. Mukamel, Selective enhancement of spectroscopic features by quantum optimal control. *Phys. Rev. Lett.* **126**, 163202 (2021).
43. A. Hosseinizadeh *et al.*, Few-fs resolution of a photoactive protein traversing a conical intersection. *Nature* **599**, 697–701 (2021).
44. D. Jadoun, M. Kowalewski, Time-resolved photoelectron spectroscopy of conical intersections with attosecond pulse trains. *J. Phys. Chem. Lett.* **12**, 8103–8108 (2021).

Downloaded from https://www.pnas.org by SCIENCE LIBRARY SERIALS on March 10, 2022 from IP address 128.200.11.4.